Atomic Spectroscopy

Article

Normalization of Laser-induced Breakdown Spectroscopy Using Laser-ablation-induced Ultrasonic Body Waves

Yuhua Hang, [a] Jinliang Zhao, [b] Shuhao Fan, [b] Lu-Ning Li, [c] Wei-Ming Xu, [c] Rong Shu, [c] Jinna Mei, [a] and Yan Qiu [b,*]

[a] Suzhou Nuclear Power Research Institute Co., Ltd., Suzhou 215004, P. R. China

[b] State Key Laboratory of Electrical Insulation and Power Equipment, Xi'an Jiaotong University, Xi'an 710049, P. R. China

[c] Key Laboratory of Space Active Opto-electronics Technology, Shanghai Institute of Technical Physics, Chinese Academy of Sciences, Shanghai 200083, P. R. China

Received: *April 21, 2026;* ***Revised:*** *September20, 2026;* ***Accepted:*** *October 05, 2026;* ***Available online:*** *October 05, 2026.*

DOI: 10.46770/AS.2026.0015s

ABSTRACT: Shot-to-shot fluctuations in laser-induced plasma emission limit the precision of quantitative laser-induced breakdown spectroscopy (LIBS). This study evaluates an ultrasonic-assisted normalization approach in which laser-ablation-induced body waves, measured with a contact piezoelectric transducer, are used as an external indicator of shot-dependent ablation variability. For each analyte, the first-arrival acoustic feature was related to the within-specimen relative deviation of the corresponding emission line using a single model fitted from pooled calibration data; the fitted coefficients were then applied unchanged to the prediction specimens. For Mn, Cr, and Cu, normalization reduced the shot-to-shot relative standard deviation (RSD) from 6.87%, 4.27%, and 4.59% to 2.30%, 2.25%, and 2.87%, respectively. The corresponding average relative errors decreased from 1.41% to 1.13% for Mn, from 2.27% to 2.02% for Cr, and from 1.04% to 0.93% for Cu. For comparison with spectral internal standardization, Fe-dominant reference features were selected from the averaged spectra using spectral non-overlap, monotonic calibration behavior, calibration-set R^2 and RMSEC, and calibration-sample RSD; prediction metrics were not used during feature selection. The selected reference features were 391.843, 427.966, and 458.218 nm for Mn, Cr, and Cu, respectively. Both the optimized Fe-ratio and ultrasonic-normalized models improved quantitative performance relative to the raw-intensity models, although the extent of improvement depended on the analyte and evaluation metric. Additional measurements showed that the body-wave response is sensitive to mechanical coupling and specimen thickness, while a synchronous comparison with an airborne-acoustic channel showed distinct temporal and statistical characteristics. Accordingly, the contact body-wave approach can serve as a configuration-dependent external reference when stable mechanical coupling can be maintained.

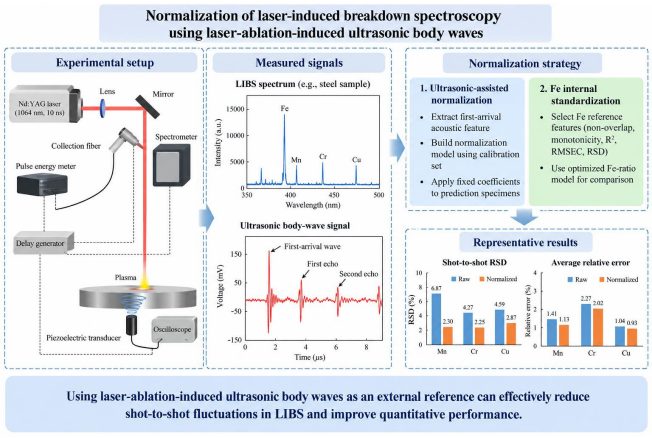

INTRODUCTION

Laser-induced breakdown spectroscopy (LIBS) provides elemental information from the optical emission of a transient laser-induced plasma and can be applied to solids, liquids, and gases.[1–3] Its minimal sample-preparation requirements, multielement capability, and compatibility with in situ and stand-off measurements have supported applications in metal classification,[4] mineral and ore analysis,[5] material identification in space applications,[6] and inspection of structural materials in the nuclear field.[7] Stand-off LIBS has also been used to relate spectral response to microstructural properties and hardness in irradiated tungsten heavy alloys.[8]

A persistent limitation in quantitative LIBS is the shot-to-shot variability of the laser-induced plasma.[9] Variations in laser-matter coupling, plasma temperature, electron density, and ablated mass alter emission intensity and reduce measurement repeatability.[10]

Self-absorption, matrix effects, and nonuniform plume evolution can further perturb the concentration-intensity relationship. Optical diagnostics have likewise identified plasma-morphology variability as an important source of signal uncertainty during the early stages of plasma evolution.[11]

Normalization is commonly used to reduce these fluctuations. Conventional approaches include full-spectrum normalization and internal-standard line ratios. Internal standardization is effective when a stable, interference-free reference line with appropriate excitation characteristics is available, but its performance can deteriorate in the presence of self-absorption, spectral interference, or differential sensitivity to plasma-state fluctuations. Non-spectroscopic observables have therefore been investigated as auxiliary descriptors of the excitation event. Plasma-imaging features have been used to improve LIBS analysis of non-flat heterogeneous samples,[12] free-space acoustic data have been fused with LIBS spectra for mineral differentiation,[13] and shock-wave parameters have been incorporated into physics-informed spectral normalization.[14] For steel analysis, an internal-standard line should also originate from an element with sufficiently stable concentration and should respond to plasma-state changes in a manner compatible with the analytical line.[15]

Acoustic measurements have a long history in laser-ablation spectroscopy. Chen and Yeung used plume-generated acoustic signals as an internal reference for laser-generated plumes,[16] and subsequent studies employed microphones, fiber-optic acoustic sensors, free-space acoustic detection, and hydrophones for normalization or multimodal analysis.[17–19] Other studies related acoustic characteristics to deposited energy, crater evolution, and matrix effects.[20–22] These approaches retain non-contact operation at the target and are therefore compatible with stand-off measurements. Acoustic monitoring has also been used in laser-ablation process control and for tracking ablated mass removal.[23,24]

The signal considered here is the elastic body wave that propagates through the specimen and is detected by a contact piezoelectric transducer. The first direct arrival can be isolated before later internal reflections and is not transmitted through the surrounding air; it is therefore less susceptible to room reverberation, airflow, and airborne ambient noise than a free-space microphone signal. This measurement, however, is conditional on a controlled specimen-transducer geometry: physical contact and stable coupling are required, stand-off capability is lost, and the measured amplitude depends on coupling condition, surface roughness, specimen thickness and geometry, acoustic impedance, internal structure, temperature, and the transducer transfer function. Coupling/thickness sensitivity tests and a synchronous body-wave/airborne-acoustic comparison were therefore included to characterize these practical dependencies; the corresponding procedures and data are given in Supplementary Sections S1 and S2. Environmental changes can also modify elastic-wave propagation in heterogeneous media, providing an additional reason to treat the contact measurement as configuration specific.[25]

Laser ablation transfers part of the deposited energy into mechanical loading of the target, generating stress waves that propagate through the solid.[26] Because the body wave and the optical emission originate from the same laser-material interaction, both may contain information related to shot-dependent changes in energy coupling and ablation. They are nevertheless governed by different transfer processes. Optical emission depends on excitation and ionization, plasma temperature, electron density, self-absorption, and collection geometry, whereas the measured body-wave amplitude is additionally filtered by elastic-wave generation and the specimen-transducer propagation path. Any optical-acoustic correlation should therefore be interpreted as an empirical relationship under a specified experimental geometry rather than as a universal one-to-one correspondence. Related laser-ultrasonic studies have also documented bulk- and surface-wave generation in the ablative regime and have used such waves for materials characterization.[27,28]

The objective of this study was to determine whether the first-arrival body-wave feature can be used as an external reference for LIBS spectral normalization under fixed coupling conditions. Emission spectra and laser-ablation-induced body waves were acquired synchronously. For each analyte, a linear relationship was fitted between the acoustic feature and the within-specimen relative deviation of the emission-line intensity using pooled calibration data. The fitted coefficients were then fixed and applied to the prediction specimens without specimen-specific refitting. Performance was evaluated in certified carbon-steel samples in terms of shot-to-shot repeatability and quantitative calibration/prediction metrics, with an analyte-specific Fe internal-standard model included as a spectral benchmark.

EXPERIMENTAL

Samples. Seven certified carbon-steel reference materials were used for quantitative analysis of Mn, Cr, and Cu (Table 1). Samples 1, 2, 4, 5, and 7 formed the calibration set, and Samples 3 and 6 were retained for independent prediction. Before measurement, the specimen surfaces were mechanically polished and cleaned with alcohol. Spectra were recorded with a 1 μs delay and a 1 ms integration time.

Instrumentation and operating conditions. Fig. 1 shows the experimental arrangement for plasma generation, optical emission acquisition, and ultrasonic detection. A Q-switched Nd:YAG laser (GRACE LASER, TINY-200L; 1064 nm, approximately 10 ns

pulse duration, 1 Hz repetition rate, 60 mJ pulse energy) was expanded and focused onto the cylindrical steel specimen to a spot diameter of approximately 0.3 mm. A plano-convex lens (L1, f = 200 mm) was used for focusing. Plasma emission was collected with an Avantes COL-UV/VIS optic (L2, f = 8.7 mm, 6 mm aperture) and recorded by an AvaSpec-ULS2048 spectrometer over 190–480 nm with an approximate spectral resolution of 0.13 nm. The body-wave signal was detected by a contact piezoelectric transducer (Ritec Inc.; 5 MHz center frequency; 91.65% fractional bandwidth at −6 dB) coupled to the lower specimen surface with ultrasonic gel and positioned beneath the ablation region. The transducer output was digitized with a Siglent SDS5000X oscilloscope. Laser and spectrometer timing were controlled by an SRS DG645 delay generator.

Synchronization and time reference. The oscilloscope was triggered by a fast photodiode that detected the laser pulse. The rising edge of the photodiode signal defined $t = 0$. Because the photodiode rise time was on the nanosecond scale, its contribution to the microsecond-scale ultrasonic timing was negligible. The spectrometer gate opened 1 μs after the trigger and remained active for 1 ms.

Ablation-position and transducer-alignment control. The initial laser-ablation position was vertically aligned with the ultrasonic transducer. For subsequent ablation positions, the transducer remained fixed and only the specimen was repositioned. The cylindrical specimen was seated in a machined hemispherical locating recess and rotated at equal angular intervals with a precision positioning mechanism. This procedure maintained a reproducible specimen-transducer geometry while fresh ablation positions were introduced.

At each fresh ablation position, 10 preliminary laser shots were used to remove surface contamination and oxide; these shots were excluded from subsequent analysis. For each specimen, 30 ablation positions were measured. At each position, 40 synchronized laser shots were recorded before moving to a fresh position, and every recorded shot produced one LIBS spectrum and one ultrasonic waveform. Thus, each specimen yielded 1,200 synchronized optical-ultrasonic shot pairs (30 positions × 40 shots), giving 8,400 paired observations across the seven specimens. Samples 1, 2, 4, 5, and 7 contributed 6,000 paired observations to the calibration set, whereas Samples 3 and 6 contributed 2,400 paired observations to the independent prediction set. For a separate fixed-position correlation test, 30 repeated laser excitations were acquired at one position of Sample 1 under fixed composition and geometry. Each excitation produced one LIBS spectrum and one ultrasonic waveform, yielding 30 synchronized single-shot pairs for correlation analysis. This correlation dataset was independent of the 1,200-pair per-specimen database used for concentration calibration and prediction.

Additional acoustic measurements were performed to quantify the dependence of the contact body-wave response on coupling condition and specimen thickness and to compare the synchronously recorded body-wave and airborne-acoustic channels. A separate coupled/uncoupled test was used to assess how coupling affected the effectiveness of body-wave normalization. The experimental details, extraction windows, and statistical results for these auxiliary measurements are reported in Supplementary (Sections S1 and S2).

Table 1. Standard carbon-steel samples for the elemental concentration analysis in wt.%

Number	Sample designation	Mn	Cr	Cu
1	GB(E)1010024a	0.65	0.085	0.042
2	ZBG056a	0.778	0.192	0.037
3	GBW(E)010291a	1.48	0.203	0.052
4	YSB37217-15	0.957	0.408	0.017
5	YSB37220-15	1.20	0.155	0.015
6	YSB37215-15	0.842	0.362	0.016
7	YSB37224-15	1.49	0.139	0.014

Note: Samples 1–3 were manufactured by Jinan Zhongbiao Science and Technology Co., Ltd., and Samples 4–7 were manufactured by Zhengzhou Research Institute of Mechanical Engineering Co., Ltd.

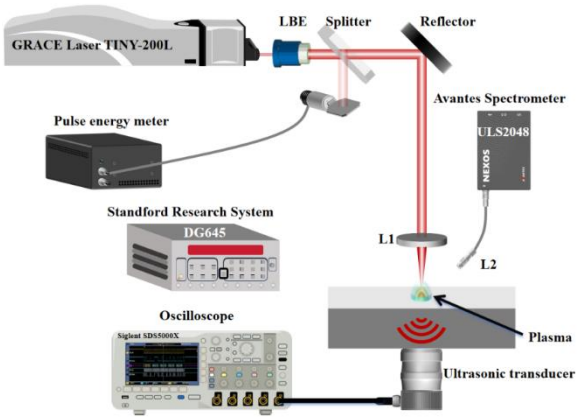

Fig. 1 Schematic of the experimental setup.

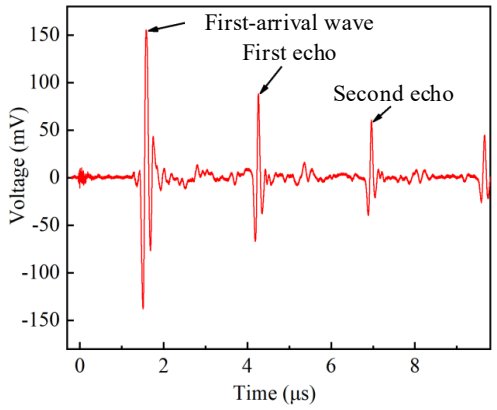

Fig. 2 Time-domain ultrasonic waveform showing the first-arrival longitudinal body wave and subsequent backwall echoes.

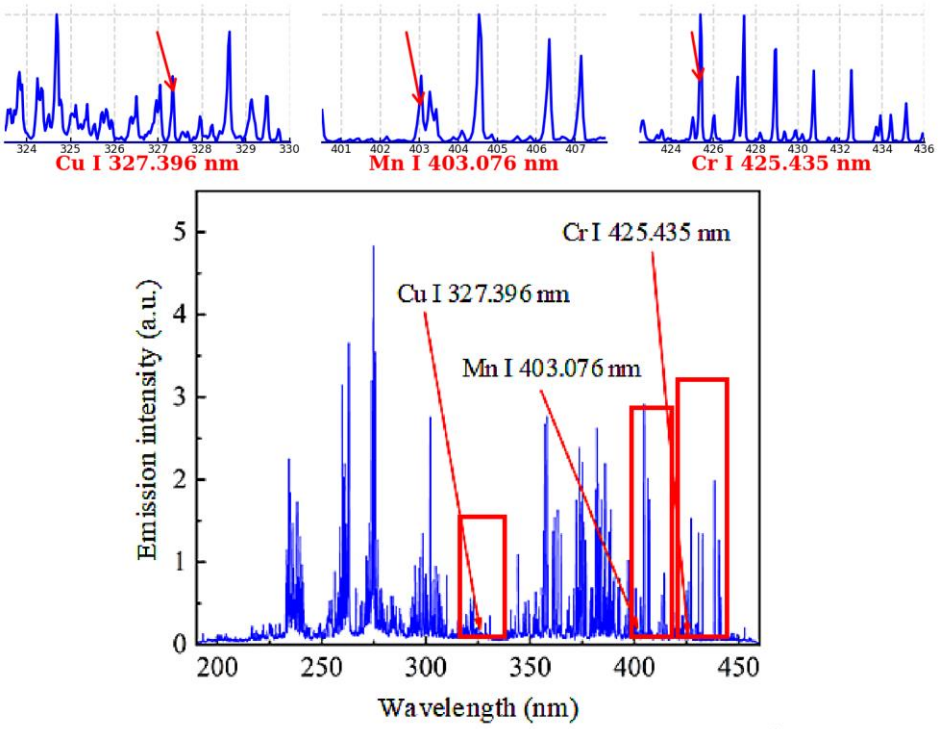

Fig. 3 Typical emission spectrum with selected lines of Mn I 403.076 nm, Cr I 425.435 nm, and Cu I 327.396 nm. The enlarged local regions above the full spectrum show the neighborhoods of the three analytical lines.

RESULTS AND DISCUSSION

Correlation analysis between ultrasonic body waves and plasma emission spectra. Fig. 2 shows a representative ultrasonic waveform from Sample 1. The first-arrival longitudinal wave was isolated within 1.45–1.76 μs after laser excitation. Two later peaks with comparable time spacing and progressively smaller amplitudes are consistent with successive backwall reflections between the upper and lower specimen surfaces. Smaller features at later times are attributed to additional reflections from specimen boundaries.

The first-arrival amplitude was sensitive to the mechanical transfer path. Removing the couplant produced a pronounced reduction in body-wave amplitude and a substantial increase in its relative variability, while increasing specimen thickness also altered both amplitude and repeatability. The 16 mm specimen showed the strongest attenuation and the largest variability among the tested thicknesses. These observations indicate that the measured first-arrival amplitude reflects contributions from both the ablation event and the specimen–transducer transfer path. The corresponding normalization test was consistent with this interpretation: with couplant, the representative spectral RSD decreased from 6.87% to 2.30% after correction, whereas the uncoupled case changed only from 6.96% to 6.27%. Stable coupling and a controlled specimen geometry are therefore necessary for using the body-wave amplitude as a reproducible auxiliary reference. Detailed data are provided in Supplementary Section S1 (Figs. S1–S2 and Table S1).

The first direct arrival was used as the acoustic feature because it precedes the later reflection sequence and can be extracted with a fixed time gate. Fig. 3 shows a representative spectrum acquired synchronously with the ultrasonic signal. Mn I 403.076 nm, Cr I 425.435 nm, and Cu I 327.396 nm were selected as analytical lines. For each line, the baseline-corrected integrated intensity was calculated over a fixed ±0.20 nm interval: 402.876–403.276 nm for Mn, 425.235–425.635 nm for Cr, and 327.196–327.596 nm for Cu. A local linear background was subtracted before integration. The acoustic feature A_i was defined as the maximum absolute baseline-corrected voltage within the fixed 1.45–1.76 μs first-arrival gate. Identical baseline and feature-extraction procedures were applied to every recorded shot.

The shot-to-shot association between integrated emission intensity and the first-arrival acoustic amplitude was quantified using Pearson's correlation coefficient:

$$r=\frac{\sum_i (I_i-\bar{I})(A_i-\bar{A})}{\sqrt{\sum_i (I_i-\bar{I})^2 \sum_i (A_i-\bar{A})^2}} \quad (1)$$

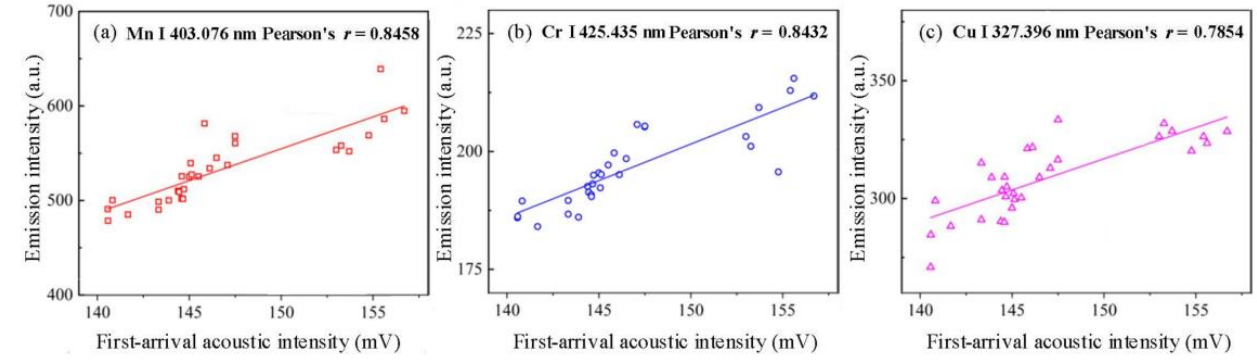

Fig. 4 Linear correlation between the first-arrival acoustic-peak amplitude and the emission-line intensity for Mn I 403.076 nm (a), Cr I 425.435 nm (b), and Cu I 327.396 nm (c). Pearson's *r* values are shown in each panel.

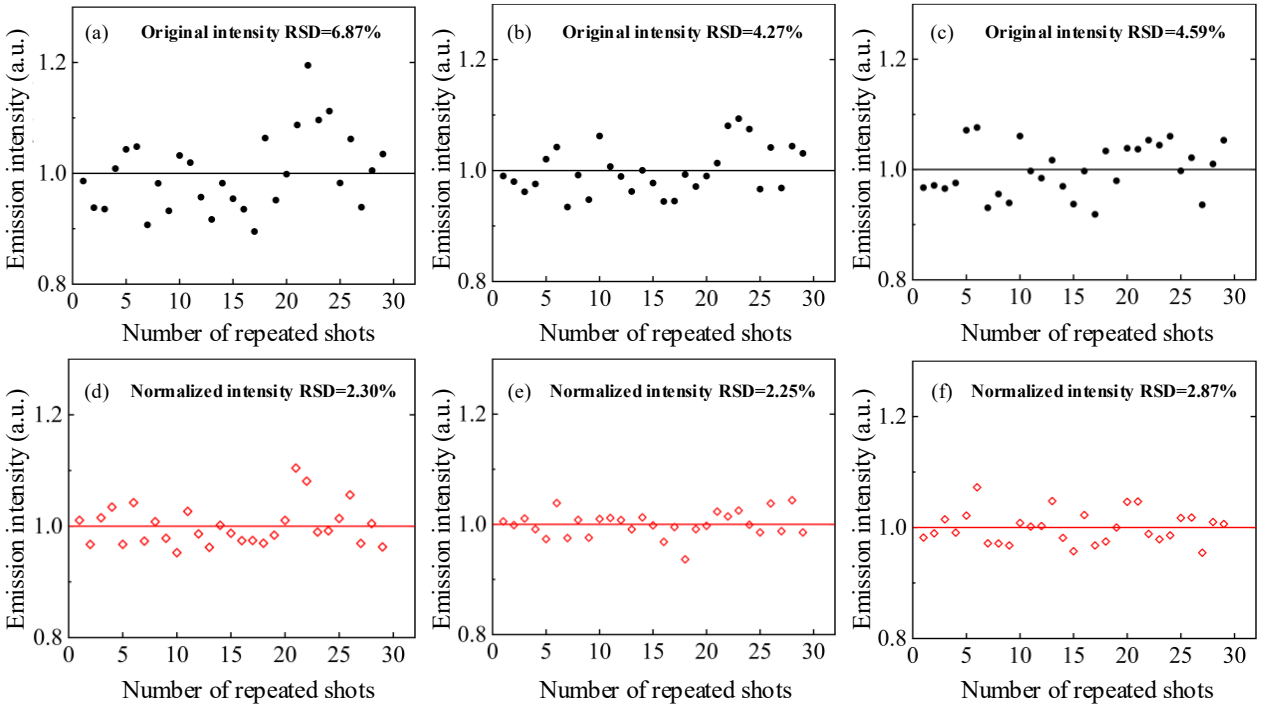

Fig. 5 Shot-to-shot spectral fluctuations of Mn I 403.076 nm, Cr I 425.435 nm, and Cu I 327.396 nm without (a-c) and with (d-f) ultrasonic-assisted normalization.

where A_i denotes the first-arrival acoustic-peak amplitude (maximum absolute baseline-corrected voltage within 1.45-1.76 μs) and I_i denotes the baseline-corrected integrated emission-line intensity obtained for shot *i*; the overbarred quantities denote the corresponding averages over repeated measurements at fixed composition. The resulting Pearson coefficients are r = 0.8458, 0.8432, and 0.7854 for Mn I 403.076 nm, Cr I 425.435 nm, and Cu I 327.396 nm, respectively (Fig. 4). Thus, the statement $r >$ 0.75 refers to within-sample shot-to-shot covariance and is not produced by pooling concentration levels.

The positive correlations are consistent with a common dependence of both observables on the laser-material interaction, but they do not establish a causal relationship. Deposited laser energy is partitioned among heating, melting, vaporization, plasma formation, and mechanical impulse; changes in the ablation process can therefore affect both the population of emitting species and the strength of the elastic-wave source.[20,23,28] The two measurements remain subject to different transfer functions. Optical emission depends on excitation and ionization conditions, plasma temperature, electron density, self-absorption, and collection geometry, whereas the measured body-wave amplitude is additionally affected by specimen thickness,

boundaries, acoustic impedance, internal structure, coupling condition, and transducer response.[21,22] These factors may contribute to differences between the optical-body-wave correlations measured here and optical-airborne-acoustic correlations reported under other experimental conditions. The present coefficients describe covariance at fixed composition, laser energy, geometry, and coupling; studies that vary energy, focus, matrix, or ablation regime probe a wider dynamic range and are not directly comparable. Accordingly, the measured optical–acoustic relationship is regarded as configuration dependent rather than universal.

For each calibration specimen, spectral fluctuation was expressed as the relative deviation of each single-shot integrated intensity from the repeated-shot mean of that same specimen. The mean in Eq. (2) was therefore calculated separately for each fixed-composition specimen and was not pooled across concentration levels. After these within-specimen deviations were obtained, the acoustic-amplitude/deviation pairs from all calibration specimens were combined to form a common training set for each analyte.

$$\varepsilon_i = \frac{I_i - \bar{I}}{\bar{I}} \quad (2)$$

The quantity defined in Eq. (2) was used as the regression response and represents the fractional departure of an individual shot from the mean response of its fixed-composition specimen.

The pooled calibration pairs were fitted with a univariate linear regression model relating the first-arrival acoustic amplitude to the spectral deviation:

$$\hat{\varepsilon}_i = aA_i + b \quad (3)$$

where, for a given analyte, a and b are the common least-squares regression coefficients estimated from the pooled calibration-specimen shots; A_i is the first-arrival acoustic-peak amplitude for shot i, and $\hat{\varepsilon_i}$ is the predicted relative deviation.

The measured intensity was converted to a mean-equivalent normalized intensity using the predicted deviation:

$$I_i^{\mathrm{nor}} = \frac{I_i}{1+\hat{\varepsilon}_i} \quad (4)$$

where I_i^{nor} is the normalized (mean-equivalent) emission-line intensity and $\hat{\varepsilon_i}$ is the predicted relative deviation calculated from Eq. (3). Equation (4) follows from $I_i = \bar{I}(1 + \varepsilon_i)$: because the mean-equivalent intensity is the unknown quantity to be estimated, it must be derived from the measured intensity by division, $I_i^{\mathrm{nor}} = I_i/(1 + \hat{\varepsilon_i})$. The unnormalized spectral intensities exhibited shot-to-shot fluctuations with RSD values of 6.87%, 4.27%, and 4.59% for Mn, Cr, and Cu, respectively. After ultrasonic-assisted normalization, the reported RSDs decreased to 2.30%, 2.25%, and 2.87%, respectively, as shown in Fig. 5.

Table 2. Study-by-study comparison of representative acoustic-assisted laser-ablation and LIBS investigations

Study and acoustic configuration	Reported optical-acoustic relation	RSD / repeatability change	Quantitative result	Target contact
Chen and Yeung (1988) [16] Metals/alloys; plasma acoustic signal peak height	Linear relation with major- and minor-element emission; numerical coefficient NR	NR	Acoustic referencing improved plume quantitation; numerical error change NR	No
Anabitarte et al. (2012) [18] Solid metal; POF acoustic sensor validated against a microphone	POF response agreed with the reference microphone; coefficient NR	NR	Improved composition estimation demonstrated; numerical error change NR	No
Huang et al. (2021) [17] Underwater solutions; immersed hydrophone; acoustic energy	Spectral intensity showed better linearity with acoustic energy than with laser energy; coefficient NR	Mean RSD_C: 5.00% to 3.18%; mean RSD_P: 5.09% to 3.28%	Calibration of Mn, Sr, and Li improved; no directly comparable ARE or RMSE value was reported	No; hydrophone immersed in water
Lu et al. (2021) [29] Coal pellets; free-space acoustic sensor; acoustic normalization factor	Strong optical-acoustic relation reported for 35-ton-compacted pellets; coefficient NR	Line RSDs: 10.16/6.53/3.79/5.21% to 7.01/4.40/2.81/3.54%; validation RSD: 6.25% to 4.16%	Validation ARE: 4.66% to 3.28%	No
Chide et al. (2019) [19] Geological targets; SuperCam microphone; shock-wave energy	Shot-to-shot links among acoustic response, crater morphology, and spectral evolution; no universal coefficient	Not evaluated as a normalization benchmark	No calibration-error benchmark reported	No
This work. Carbon steels; contact piezoelectric transducer; first-arrival peak amplitude	Pearson r = 0.8458 (Mn), 0.8432 (Cr), and 0.7854 (Cu)	RSD: 6.87/4.27/4.59% to 2.30/2.25/2.87%	ARE: 1.41/2.27/1.04% to 1.13/2.02/0.93%; RMSEC and RMSEP also decreased	Yes

Note: NR indicates that the cited study did not report the corresponding metric in a directly comparable form. RSD_C and RSD_P denote average relative standard deviations for calibration and prediction samples, respectively.

A single pair of coefficients a and b was fitted for each analyte from the pooled synchronized shots of Samples 1, 2, 4, 5, and 7. The response variable for each shot was first referenced to the mean of its own specimen through Eq. (2), after which all calibration-specimen pairs were combined for least-squares fitting. The fitted coefficients were then fixed and applied directly to Samples 3 and 6. No concentration information or specimen-specific coefficient fitting from the prediction samples entered the ultrasonic correction.

Under the fixed experimental geometry, body-wave normalization reduced within-specimen spectral variability for all three analytical lines. Because the acoustic feature is measured independently of the emission spectrum, this approach does not require an additional spectral reference line and may be useful when an appropriate internal reference is unavailable or affected by interference or self-absorption. The method also introduces an additional measurement channel and depends on reproducible mechanical coupling. It is therefore considered complementary to spectral normalization rather than a general replacement for it.

Comparison with previous acoustic-assisted LIBS studies. Table 2 summarizes representative studies that used acoustic information in laser-ablation or LIBS measurements, including sensor configuration, reported optical-acoustic relationships, changes in repeatability, quantitative performance, and target-contact requirements.[16–19,29] Direct numerical comparison is limited because the studies differ in sample type, sensor response, acoustic feature definition, imposed perturbations, and validation design. Metrics that were not reported in a comparable form are therefore listed as NR rather than estimated.

The contact body-wave and airborne-acoustic channels were also recorded synchronously under the same excitation conditions. Their temporal waveforms and shot-to-shot statistics differed, consistent with the different generation, propagation, and detection paths of the two measurements. Under the present configuration, the body-wave channel provided an earlier, temporally localized response and a slightly higher mean SNR, whereas the airborne-acoustic channel exhibited lower peak-amplitude RSD and retained non-contact operation. No significant shot-to-shot covariance was observed for paired peak amplitude, RMS, or energy features. This comparison characterizes the two acoustic channels at the signal level only; synchronous LIBS spectra were not recorded in this auxiliary experiment, so normalization performance was not compared. The paired data and statistical results are reported in Supplementary Section S2 (Fig. S3 and Tables S2–S4).

Quantitative spectroscopic analysis. Calibration curves for Mn, Cr, and Cu were constructed with Samples 1, 2, 4, 5, and 7; Samples 3 and 6 were used only for independent prediction (Fig. 6). Three response variables were evaluated: the raw baseline-corrected integrated intensity, the ultrasonic-normalized intensity from Eq. (4), and an analyte/Fe intensity ratio. For the internal-standard model, a grand-average spectrum constructed from all recorded spectra was used only to identify sufficiently prominent candidate peaks over 190–480 nm. This unsupervised peak-detection step used spectral intensity information only; concentration labels and prediction-set performance metrics were not used. Candidates within 0.50 nm of Mn I 403.076 nm, Cr I 425.435 nm, or Cu I 327.396 nm were excluded to avoid direct overlap with the analytical lines. Both the analytical lines and the candidate Fe-dominant features were integrated over fixed ±0.20 nm windows after local baseline correction, and the analyte/Fe ratio was calculated separately for each shot. Only candidates that produced a monotonic calibration response over the investigated concentration range were retained. Final selection used calibration-set R^2, RMSEC, and the RSD of the calibration-sample ratios; RMSEP and prediction ARE were calculated only after the reference feature had been fixed. The resulting Fe-dominant reference features were 391.843 nm for Mn, 427.966 nm for Cr, and 458.218 nm for Cu. For each specimen, the plotted response represents the mean of the repeated-shot ratios, and the error bar denotes the corresponding standard deviation. The raw-intensity, ultrasonic-normalized, and Fe-ratio models were fitted using the same calibration/prediction split and the same second-order polynomial form so that differences among the three responses were not confounded by model order or sample allocation.

$$I_{X,i}^{\mathrm{IS}} = \frac{I_{X,i}}{I_{\mathrm{Fe},X,i}} \tag{5}$$

where $I_{X,i}^{IS}$ is the Fe internal-standard(IS) intensity ratio for analyte X in shot i; $I_{X,i}$ is the baseline-corrected integrated emission-line intensity of analyte X in shot i; $I_{\mathrm{Fe},X,i}$ is the baseline-corrected integrated intensity of the selected Fe-dominant reference feature for the same analyte and shot (391.843, 427.966, or 458.218 nm for Mn, Cr, and Cu, respectively); X denotes Mn, Cr, or Cu; and i is the shot index. The ratio is dimensionless.

Quantitative errors were calculated from concentrations obtained by inverse calibration. ARE was the mean absolute relative difference between the predicted and certified concentrations. RMSEC was calculated for Samples 1, 2, 4, 5, and 7 ($n_c = 5$), and RMSEP for Samples 3 and 6 ($n_p = 2$). RMSEC and RMSEP are reported in 10^{-3} wt.%. For inversion of the quadratic calibration, the physically admissible root within the certified concentration range was used.

Figure 6 and Table 3 compare the three response strategies using the same calibration/prediction split. For Mn, ultrasonic normalization increased R^2 from 0.9891 to 0.9933 and reduced ARE from 1.41% to 1.13%, RMSEC from 10.67 to 8.434, and RMSEP from 12.41 to 9.945. The Mn/Fe ratio based on the 391.843 nm reference feature produced $R^2 = 0.9954$, ARE = 0.65%,

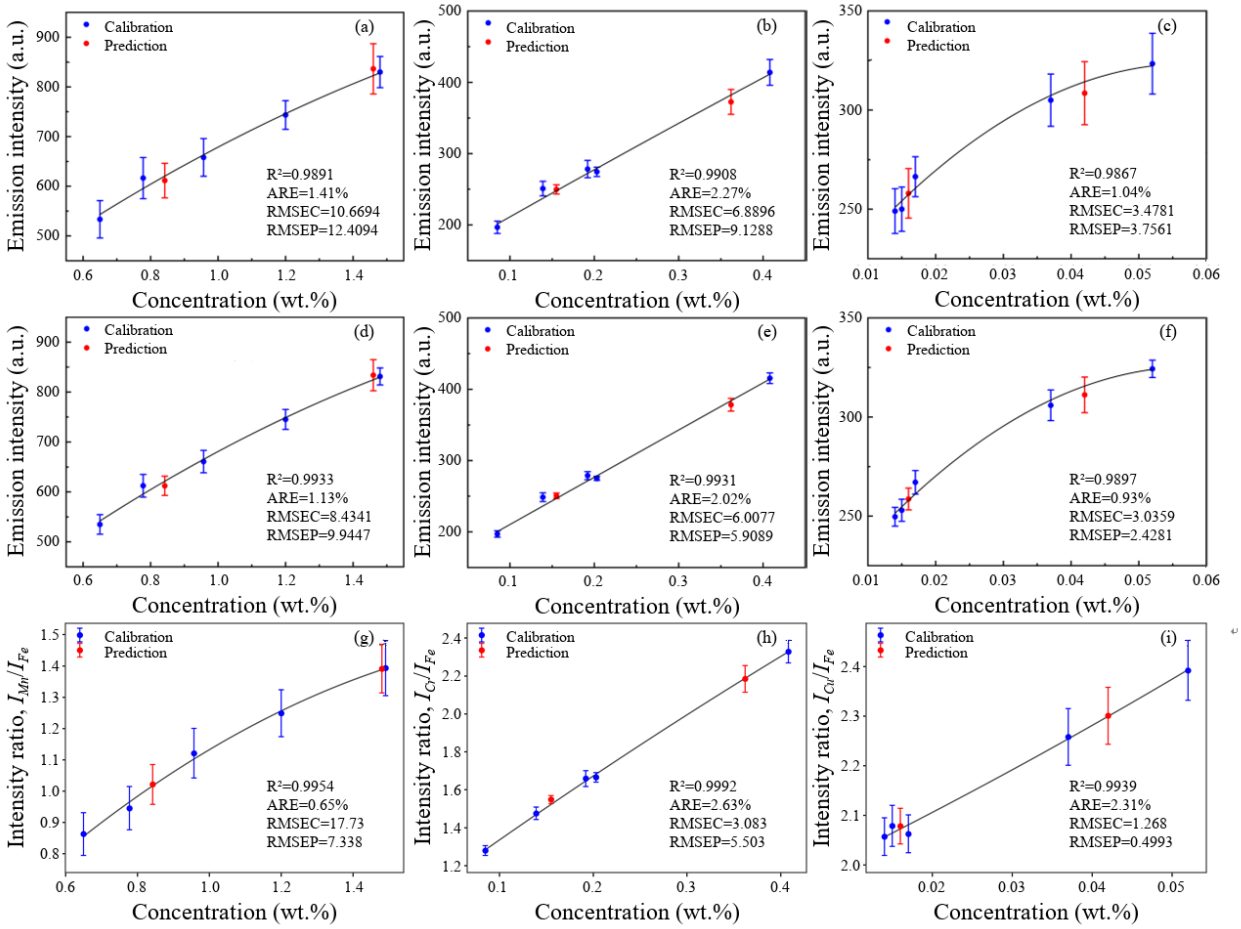

Fig. 6 Calibration and prediction curves for Mn I 403.076 nm, Cr I 425.435 nm, and Cu I 327.396 nm obtained using raw emission intensities (a–c), ultrasonic-assisted normalization (d–f), and Fe-dominant internal-standard intensity ratios selected by full-range candidate screening (g–i), respectively. The selected Fe-dominant reference features were 391.843 nm for Mn, 427.966 nm for Cr, and 458.218 nm for Cu. Samples 1, 2, 4, 5, and 7 were used for calibration, whereas Samples 3 and 6 were used for independent prediction in all nine panels. Blue symbols represent calibration samples, red symbols represent prediction samples, and error bars indicate the standard deviations of repeated measurements. For the Fe internal-standard model, the vertical axes in panels (g–i) represent the dimensionless analyte-to-Fe intensity ratios. Numerical values of R2, ARE, RMSEC, and RMSEP are shown in the panels and summarized in Table 3. ARE is expressed in %, whereas RMSEC and RMSEP are reported in units of 10^{-3} wt.%.

Table 3. Quantitative performance of the raw-intensity, ultrasonic-assisted, and Fe internal-standard calibration models. RMSEC and RMSEP are reported in 10^{-3} wt.%

Element	Metric	Raw	Ultrasonic-normalized	Fe internal-standard
Mn	R^2	0.9891	0.9933	0.9954
	ARE (%)	1.41	1.13	0.65
	RMSEC	10.67	8.434	17.73
	RMSEP	12.41	9.945	7.338
Cr	R^2	0.9908	0.9931	0.9992
	ARE (%)	2.27	2.02	2.63
	RMSEC	6.89	6.008	3.083
	RMSEP	9.129	5.909	5.503
Cu	R^2	0.9867	0.9897	0.9939
	ARE (%)	1.04	0.93	2.31
	RMSEC	3.478	3.036	1.268
	RMSEP	3.756	2.428	0.4993

RMSEC = 17.73, and RMSEP = 7.338 (RMSEC and RMSEP in 10^{-3} wt.%). Thus, the Fe-ratio model yielded the highest R^2 and the lowest ARE and RMSEP for Mn, whereas the ultrasonic model yielded the lowest RMSEC. The two normalization schemes therefore improved different aspects of the Mn calibration relative to the raw-intensity response.

For Cr, ultrasonic normalization increased R^2 from 0.9908 to 0.9931 and reduced ARE, RMSEC, and RMSEP from 2.27%, 6.89, and 9.129 to 2.02%, 6.008, and 5.909, respectively. Using the 427.966 nm Fe-dominant feature increased R^2 to 0.9992 and reduced RMSEC and RMSEP to 3.083 and 5.503, while ARE was 2.63%. The Fe-ratio model therefore yielded the highest R^2 and the lowest RMSEC and RMSEP values, whereas the ultrasonic model yielded the lowest ARE.

For Cu, ultrasonic normalization increased R^2 from 0.9867 to 0.9897 and reduced ARE, RMSEC, and RMSEP from 1.04%, 3.478, and 3.756 to 0.93%, 3.036, and 2.428, respectively. The Cu/Fe ratio based on the 458.218 nm reference feature produced $R^2 = 0.9939$, RMSEC = 1.268, and RMSEP = 0.4993, while ARE was 2.31%. The Fe-ratio model therefore yielded the highest R^2 and the lowest RMSEC and RMSEP values, whereas the ultrasonic model yielded the lowest ARE. Because the Cu concentrations are small, modest absolute concentration differences can produce comparatively large relative errors.

The analyte-specific Fe references provided a more competitive internal-standard benchmark than a single common Fe line. Across the three analytes, the Fe-ratio models yielded the highest R^2 values and the lowest RMSEP values, while the ultrasonic model yielded the lowest Mn RMSEC and the lowest ARE values for Cr and Cu. The relative performance therefore depends on both analyte and evaluation metric. These data do not support treating the body-wave approach as universally superior to internal standardization. Instead, the body wave provides an independent external normalization variable that can be used when a suitable spectral reference is unavailable, subject to the requirement for stable coupling and a controlled acoustic propagation path.

CONCLUSION

Laser-ablation-induced ultrasonic body waves served as an external normalization variable for LIBS under a fixed contact-coupling geometry. For each analyte, a single acoustic-deviation model fitted from the pooled calibration specimens was applied unchanged to the prediction specimens. The resulting normalization reduced the shot-to-shot RSD of Mn, Cr, and Cu from 6.87%, 4.27%, and 4.59% to 2.30%, 2.25%, and 2.87%, respectively, and reduced ARE, RMSEC, and RMSEP relative to the corresponding raw-intensity models. An analyte-specific Fe internal-standard comparison, selected using only calibration-set criteria, yielded the highest R^2 and lowest RMSEP for the three analytes, whereas the ultrasonic model yielded the lowest Mn RMSEC and the lowest ARE values for Cr and Cu. The two normalization strategies therefore emphasize different performance characteristics rather than showing a single method to be superior for all analytes and metrics. The auxiliary coupling experiments also identified a practical constraint of the contact approach: correction was effective with stable coupling (RSD 6.87% to 2.30%) but was substantially weaker without couplant (6.96% to 6.27%). The body-wave and airborne-acoustic channels further exhibited different timing and variability characteristics, consistent with their different propagation paths. For applications that permit stable target contact, the first-arrival body wave can therefore serve as a non-spectroscopic reference for reducing LIBS intensity fluctuations; extension to stand-off use will require direct normalization comparisons with simultaneously acquired airborne-acoustic and LIBS signals.

ASSOCIATED CONTENT

The supporting information (Section S1. Coupling/thickness sensitivity and coupling-dependent normalization performance, Section S2. Synchronous comparison of body-wave and airborne-acoustic signals, Figs. S1−S3 and Tables S1−S4) is available at https://www.at-spectrosc.com

AUTHOR INFORMATION

Yan Qiu was born in Shandong, China, in 1993. He received the B.S. degree in electrical engineering from Southwest Jiaotong University, Chengdu, China, in 2016, and the Ph.D. degree in electrical engineering from Xi'an Jiaotong University, Xi'an, China, in 2021. He is currently an Associate Professor with Xi'an Jiaotong University. His research interests include Laser-Induced Breakdown Spectroscopy.

Corresponding Authors

* Y. Qiu

Email address: qiuyan@xjtu.edu.cn

Notes

The authors declare no competing financial interest.

ACKNOWLEDGMENTS

The authors acknowledge financial support from the National Natural Science Foundation of China (62575236) and the Fundamental Research Funds for the Central Universities (xzy012026029)

REFERENCES

1. V. Palleschi, S. Legnaioli, F. Poggialini, F. O. Bredice, I. A. Urbina, N. Lellouche, and S. M. Aberkane, *Nat. Rev. Methods Primers*, 2025, **5**, 17. https://doi.org/10.1038/s43586-025-00388-w
2. D. W. Hahn and N. Omenetto, *Appl. Spectrosc.*, 2010, **64**, 335A–366A. https://doi.org/10.1366/000370210793561691
3. S. Liu, Y. Liu, B. Xu, B. Lei, S. Ran, Y. Wang, Y. Duan, W.-R. Zhao, and J. Tang, *Appl. Opt.*, 2022, **61**, 3008–3018. https://doi.org/10.1364/AO.451217
4. G. Chen, Q. Zeng, W. Li, X. Chen, M. Yuan, L. Liu, H. Ma, B.

Wang, Y. Liu, L. Guo, and H. Yu, *Opt. Express*, 2022, **30**, 9428–9440. https://doi.org/10.1364/OE.451969

5. A. Li, X. Zhang, X. Liu, Y. He, Y. Shan, H. Sun, W. Yi, and R. Liu, *Opt. Express*, 2023, **31**, 38728–38743. https://doi.org/10.1364/OE.505574
6. H. Saeidfirozeh, P. Kubelík, V. Laitl, A. Křivková, J. Vrábel, K. Rammelkamp, S. Schröder, I. B. Gornushkin, E. Képeš, J. Žabka, M. Ferus, P. Pořízka, and J. Kaiser, *TrAC Trends Anal. Chem.*, 2024, **181**, 117991. https://doi.org/10.1016/j.trac.2024.117991
7. Y. Qiu, J. Li, B. Lu, J. Wu, X. Guo, Y. Hang, Y. Li, and X. Li, *J. Anal. At. Spectrom.*, 2024, **39**, 3048–3059. https://doi.org/10.1039/D4JA00291A
8. H. Sattar, J. Shi, H. Ran, M. Imran, W. Ding, P. D. Gupta, and H. Ding, *J. Nucl. Mater.*, 2020, **540**, 152389. https://doi.org/10.1016/j.jnucmat.2020.152389
9. H. Qin, Z. Yu, Z. Lu, Z. Yu, and S. Yao, *Appl. Spectrosc.*, 2022, **76**, 1123–1131. https://doi.org/10.1177/00037028221108416
10. E. Tognoni and G. Cristoforetti, *Opt. Laser Technol.*, 2016, **79**, 164–172. https://doi.org/10.1016/j.optlastec.2015.12.010
11. Y.-T. Fu, W.-L. Gu, Z.-Y. Hou, S. A. Muhammed, T.-Q. Li, Y. Wang, and Z. Wang, *Front. Phys.*, 2021, **16**, 22502. https://doi.org/10.1007/s11467-020-1006-0
12. V. N. Lednev, P. A. Sdvizhenskii, A. S. Dorohov, S. M. Pershin, and S. V. Gudkov, *Appl. Opt.*, 2023, **62**, 2030–2038. https://doi.org/10.1364/AO.473111
13. C. Alvarez-Llamas, P. Purohit, J. Moros, and J. J. Laserna, *Anal. Chem.*, 2022, **94**, 1840–1849. https://doi.org/10.1021/acs.analchem.1c04792
14. Y. Zhou, J. Wu, M. Shi, M. Chen, C. Pei, X. Guo, Y. Hang, J. Li, and X. Li, *Appl. Phys. Lett.*, 2025, **126**, 034103. https://doi.org/10.1063/5.0237618
15. P. Zheng, H. Zhang, J. Wang, G. Chen, P. Dai, H. Huang, and L. Guo, *J. Anal. At. Spectrom.*, 2026, **41**, 1032–1041. https://doi.org/10.1039/D5JA00470E
16. G. Chen and E. S. Yeung, *Anal. Chem.*, 1988, **60**, 2258–2263. https://doi.org/10.1021/ac00171a020
17. F. Huang, Y. Tian, Y. Lu, et al., *Appl. Opt.*, 2021, **60**, 1595–1602. https://doi.org/10.1364/AO.413853
18. F. Anabitarte, L. Rodríguez-Cobo, J.-M. López-Higuera, and A. Cobo, *Appl. Opt.*, 2012, **51**, 8306–8314. https://doi.org/10.1364/AO.51.008306
19. B. Chide, S. Maurice, N. Murdoch, J. Lasue, B. Bousquet, X. Jacob, A. Cousin, O. Forni, O. Gasnault, P.-Y. Meslin, J.-F. Fronton, M. Bassas-Portús, A. Cadu, A. Sournac, D. Mimoun, and R. C. Wiens, *Spectrochim. Acta B*, 2019, **153**, 50–60. https://doi.org/10.1016/j.sab.2019.01.008
20. W. Wu, S. Chai, and Y. Zhou, *Appl. Opt.*, 2022, **61**, 1734–1742. https://doi.org/10.1364/AO.442780
21. W. Wu, S. Chai, and Y. Zhou, *Appl. Opt.*, 2023, **62**, 9375–9382. https://doi.org/10.1364/AO.506394
22. M. Bosáková, K. Novotný, J. Moros, and J. J. Laserna, *Spectrochim. Acta B*, 2025, **226**, 107140. https://doi.org/10.1016/j.sab.2025.107140
23. A. Papanikolaou, G. J. Tserevelakis, K. Melessanaki, C. Fotakis, G. Zacharakis, and P. Pouli, *Opto-Electron. Adv.*, 2020, **3**, 190037. https://doi.org/10.29026/oea.2020.190037
24. S. Kradolfer, K. Heutschi, J. Koch, and D. Günther, *Spectrochim. Acta B*, 2021, **179**, 106118. https://doi.org/10.1016/j.sab.2021.106118
25. L. Gao, P. Shokouhi, and J. Rivière, *J. Appl. Phys.*, 2022, **131**, 055101. https://doi.org/10.1063/5.0073967
26. X. Hu, Y. Ma, Q. Wan, K.-N. Ying, L.-N. Dai, Z. Hu, F. Chen, F. Guan, C. Ni, and L. Guo, *Appl. Opt.*, 2022, **61**, 4145–4152. https://doi.org/10.1364/AO.454888
27. R. H. Buzolin, M. C. M. Rodrigues, M. Militzer, A. Krumphals, E. Guntsche, S. Sommadossi, and M. C. Poletti, *Mater. Today Commun.*, 2023, **37**, 107364. https://doi.org/10.1016/j.mtcomm.2023.107364
28. T. T. P. Nguyen, R. Tanabe-Yamagishi, and Y. Ito, *Phys. Lett. A*, 2023, **464**, 128692. https://doi.org/10.1016/j.physleta.2023.128692
29. P. Lu, Z. Zhuo, W. Zhang, et al., *Appl. Phys. B*, 2021, **127**, 82. https://doi.org/10.1007/s00340-021-07626-5